PNAS
www.pnas.org

Supplementary Information for

Hyperpolarized Xe NMR Signal Advancement by Metal-Organic Framework Entrapment in Aqueous Solution

Qingbin Zeng[†‖], Binglin Bie[‡‖], Qianni Guo[†¶*], Yaping Yuan[†¶], Qi Han[‡], Xiaocang Han[§], Mingwei Chen[§], Xu Zhang[†¶], Yunhuang Yang[†¶], Maili Liu[†¶], Pan Liu[§], Hexiang Deng[‡#*], Xin Zhou[†¶*]

[†]Key Laboratory of Magnetic Resonance in Biological Systems, State Key Laboratory of Magnetic Resonance and Atomic and Molecular Physics, National Center for Magnetic Resonance in Wuhan, Wuhan Institute of Physics and Mathematics, Innovation Academy for Precision Measurement Science and Technology, Chinese Academy of Sciences-Wuhan National Laboratory for Optoelectronics, Wuhan, 430071, P. R. China.
[‡]Key Laboratory of Biomedical Polymers-Ministry of Education, College of Chemistry and Molecular Sciences, Wuhan University, Wuhan, 430072, P. R. China.
[¶]University of Chinese Academy of Sciences, Beijing, 100049, P. R. China.
[§]State Key Laboratory of Metal Matrix Composites, School of Materials Science and Engineering, Shanghai Jiao Tong University, Shanghai, 200240, P. R. China.
[#]The Institute of Advanced Studies, Wuhan University, Wuhan, 430072, P. R. China.

*Xin Zhou; Hexiang Deng; Qianni Guo
Email: xinzhou@wipm.ac.cn; hdeng@whu.edu.cn; qian-niguo@wipm.ac.cn

This PDF file includes:

www.pnas.org/cgi/doi/10.1073/pnas.2004121117

Supplementary Information Text

Section S1

Chemicals

Zinc nitrate tetrahydrate ($Zn(NO_3)_2$•$4H_2O$), zinc nitrate hexahydrate ($Zn(NO_3)_2$•$6H_2O$), zinc acetate dehydrate ($Zn(OAc)_2$•$2H_2O$), N, N-dimethylformamide (DMF), anhydrous methanol (MeOH), 2-methyl-imidazole (mIM), 1-methyl-imidazole, n-butylamine were purchased from Sinopharm Chemical Reagent Co. Ltd (China). All chemicals were used without further purification unless otherwise mentioned.

Synthesis of ZIF-8 and ZIF-7

Synthesis of ZIF-8 with n-butylamine or 1-methylimidazole as modulators

The synthesis of ZIF-8 with the assistance of n-butylamine and 1-methylimidazole followed the literature report (1). $Zn(NO_3)_2{\cdot}6H_2O$ (734.4 mg, 2.47 mmol) was dissolved in 50 mL MeOH using ultrasound in a 250 mL conical flask. While mIM (810.6 mg, 9.87 mmol) and 1-methylimidazole (810.6 mg, 9.87 mmol) was dissolved in 50 mL of MeOH using ultrasound in a 250 mL conical flask. The latter solution was poured into the former solution under vigorous stirring. Stirring was stopped as soon as the solution was fully mixed with the solution of zinc salt. Then, the mixture was left standing for 24 h before the white precipitate was centrifuged from the solution. The product was washed with MeOH three times to remove the unreacted metal salts and ligands. The synthesis with n-butylamine is similar to the procedures above, with the 1-methylimidazole was replaced by n-butylamine (0.975 mL, 9.874 mmol), while the other reactants remained the same.

Synthesis of ZIF-8 without modulator

The synthesis of ZIF-8 without the assistance of modulators followed the literature report (1). $Zn(NO_3)_2{\cdot}6H_2O$ (734.4 mg, 2.47 mmol) and mIM (810.6 mg, 9.87 mmol) were each completely dissolved in 50 mL of MeOH using ultrasound in separate 250 mL conical flasks. The latter solution was poured into the former solution under vigorous stirring. Stirring was stopped as soon as the solution was fully mixed. The mixture was left standing for 24 h before the white precipitate was centrifuged from the solution. The product was washed with MeOH three times to remove the unreacted metal salts and ligands.

Synthesis of ZIF-8 with $Zn(OAc)_2$•$2H_2O$ or $Zn(NO_3)_2$•$6H_2O$

The synthesis of ZIF-8 with the assistance of $Zn(OAc)_2$•$2H_2O$ or $Zn(NO_3)_2$•$6H_2O$ followed the literature report (1). $Zn(NO_3)_2$•$6H_2O$ (300 mg, 1 mmol) was dissolved in 14 mL MeOH. The solution of mIM (660 mg, 8.05 mmol) dissolved in 14 mL MeOH was added to the $Zn(NO_3)_2$ solution followed by vigorous stirring for 3 h. The molar ratio of Zn salt is the same for $Zn(OAc)_2$•$2H_2O$, and the reaction time for the synthesis was reduced to 1.5 h. The product was washed with MeOH three times to remove the unreacted metal salts and ligands.

Sample activation procedures of ZIF-8 samples

The as-synthesized samples of ZIF-8 were centrifuged and washed three times with anhydrous MeOH. The resulting MeOH-exchanged samples were transferred as suspension to a quartz cell followed by solvent decantion. The MeOH in the pores was removed by evacuating the ZIF-8 samples (10^{-2} Torr) at room temperature for 12 h followed by heating at 120 °C for 12 h at the rate of 1 °C/min in both the heating and cooling process.

Synthesis of ZIF-7 nanoparticles

$Zn(NO_3)_2$•$6H_2O$ (136 mg, 0.5 mmol) was dissolved in 5 mL DMF, and benzimidazole (120 mg, 1 mmol) was dissolved in 5 mL MeOH. The solution of metal salts was then added to the MeOH solution quickly. After reaction for 30 min, the ZIF-7 nanocrystals were collected by centrifugation (10,000 rpm, 10 min).

Section S2

DLS analysis

Particle size distribution

Particle size was measured by laser doppler micro-electrophoresis (DLS) using a Zetasizer Nano-ZS, from Malvern UK. The results were shown in Figs. S1-S5 and Table S1.

Section S3

Electron Microscopy Imaging

Scanning Electron Microscopy (SEM) imaging of ZIF-7

ZIF-7 and ZIF-8 samples were ground slightly and SEM was performed on a FEI Varios, with accelerating voltage of 0.5 kV.

Transmission Electron Microscopy (TEM) imaging of ZIF-8 nanocrystals

ZIF-8 samples were dispersed in MeOH and sonicated for 5 s. The sample dispersion was then dropped on to the ultrathin carbon film. The TEM was performed on a Cs-corrected JEM-ARM200F with accelerating voltage of 200 kV.

Once the particles of ZIF-8 grew to around 100 nm, the crystallinity dramatically increased with the morphology becoming more completed and ordered. Lattice fringes of ZIF-8 nanocrystals around 100 nm were also clearly revealed in TEM images, demonstrating the high crystallinity of ZIF-8 nanocrystals (Figs. S8 and S9).

Section S4

X-ray Diffraction Crystallography

The Powder X-ray Diffraction (PXRD) data of ZIF-8 were collected on a Rigaku Smartlab diffractometer (Cu Ka). From the PXRD pattern, the nanocrystal structure of ZIF-8 was in accordance with the simulated pattern (Fig. S11), in which the peak width increased with the decrease of crystal size. At the same time, the PXRD pattern was also acquired after the ZIF-8 (110 nm) immersion in water for 24 h. The nearly unaltered diffractions indicated that the integrity of ZIF-8 was largely maintained (Fig. S12).

The PXRD data of ZIF-7 were collected on a Rigaku Smartlab diffractometer (Cu Ka). From the PXRD pattern, the nanocrystal structure of ZIF-7 was in accordance with the simulated pattern (Fig. S13).

Section S5

Thermal gravimetric analysis (TGA)

All measurements were performed on a TGA Q500 thermal gravimetric analyzer with samples held in aluminum oxide pans in a continuous airflow atmosphere (Balance gas: N_2: 40.0 mL/min, Sample gas: Air: 60.0 mL/min). The samples were heated at a constant rate of 10 °C during all TGA experiments. The result was shown in Fig. S14.

Section S6

N_2 adsorption analysis

All N_2 adsorption experiments were performed on a Quantachrome Autosorb-1 automatic volumetric instrument. A liquid nitrogen bath (77 K) was used for isotherm measurements. Ultra-high purity grade N_2 was used for the adsorption experiments. The Brunauer-Emmett-Teller (BET) analysis was performed by plotting $x/v(1-x)$ vs x, where $x = P/P_0$ (P_0 = 1 bar) and v was the volume of nitrogen adsorbed per gram of MOF at standard temperature and pressure (STP). This analysis produced a curve typically consisting of three regions: concave to the x axis at low pressures, linear at intermediate pressures, and convex to the x axis at high pressures. The slope ($[c-1]/v_m c$) and y intercept ($1/v_m c$) of this linear region gave the monolayer capacity, v_m, that was then used to calculate the surface area from $A = v_m \sigma_0 N_{AV}$, where σ_0 was the cross-section. All area of the adsorbate at liquid density (16.2 $Å^2$ for nitrogen) and N_{AV} was Avogadro's number (2).

Pore size distributions for MOFs were analyzed using quenched non-local density functional theory (NLDFT) based on a carbon model containing slit pores (Fig. S15-S25).

Section S7

Infrared Spectra and Raman Spectra of ZIF-8

Infrared (IR) spectra of ZIF-8

All IR spectra were recorded on a Thermo Nicolet iS10 IR spectrometer made by Thermofisher, samples were tableted and KBr was utilized as background. The wavelength range is 4000 cm^{-1} to 500 cm^{-1} (Fig. S26).

Raman Spectra of ZIF-8

All Raman spectra were recorded on a Reinshaw inVia with an excitation wavelength of 532 nm (Fig. S27).

Section S8

Hyperpolarized ^{129}Xe NMR/MRI

Hyperpolarized ^{129}Xe gas was generated using a home-built ^{129}Xe hyperpolarizer (hyperpolarized ^{129}Xe nuclear spin polarization was 100,000 times greater than its thermal equilibrium polarization). All ^{129}Xe NMR/MRI experiments used a 9.4 T Bruker AV400 wide bore NMR spectrometer (Bruker Biospin, Ettlingen, Germany). A gas mixture of 10% N_2, 88% He, and 2% Xe (26.4% ^{129}Xe natural abundance) (Spectra Gases) was used. Using the pressure from the polarizer (3.5 bar), the gas flow is 0.12 SLPM, and the gas mixture was directly bubbled into the sample solution by using a spectrometer triggered bubble dispenser. The results were shown in Figs. S28 to S32.

Section S9

PXRD pattern of pristine ZIF-8 and ^{129}Xe loaded ZIF-8

The results were shown in Figs. S33 and S34.

Section S10

The morphology comparison of ZIF-7 and ZIF-8

Based on the single crystal structure of ZIF-8 reported (3), two kinds of window sizes are observed (Fig. S35), a four-membered ring in [100] direction and a six-membered ring in [111] direction. The four-membered ring exhibits a negligible aperture for the entrance of Xe atoms, while the six-membered ring that is close to the Xe diameter and possesses enough flexibility to let the Xe enter into pores. From a previous study (4), the diameter of the six-membered ring (window size) is 3.8 Å, but the flexibility of the structure allows for an effective diameter from 3.8 Å to 4.3 Å , which suitable for the Xe (4.30 Å) enter into the pores of ZIF-8.

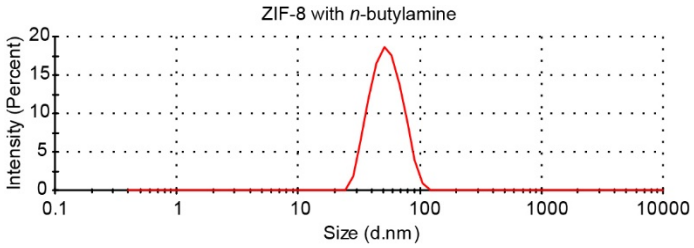

Fig. S1. DLS size distribution of ZIF-8 modulated by n-butylamine in MeOH dispersion.

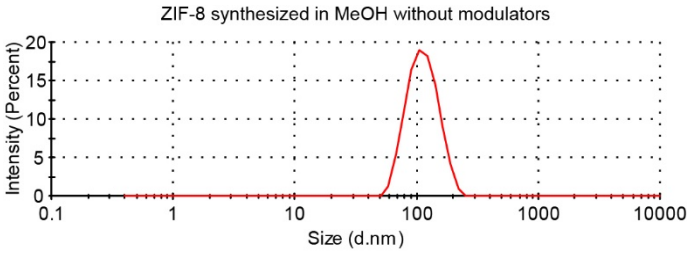

Fig. S2. DLS size distribution of ZIF-8 without modulators in MeOH dispersion.

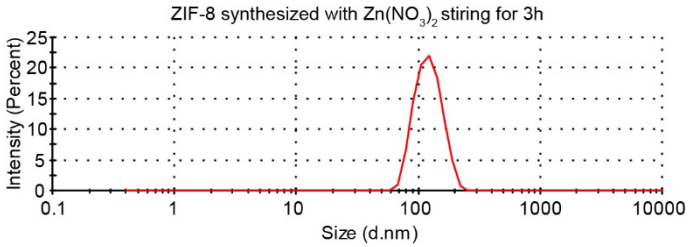

Fig. S3. DLS size distribution of ZIF-8 with stirring in MeOH dispersion.

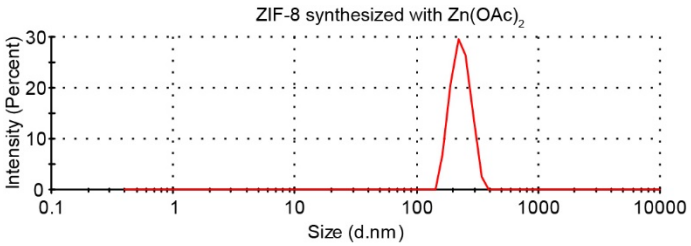

Fig. S4. DLS size distribution of ZIF-8 (synthesized with $Zn(OAc)_2$) in MeOH dispersion.

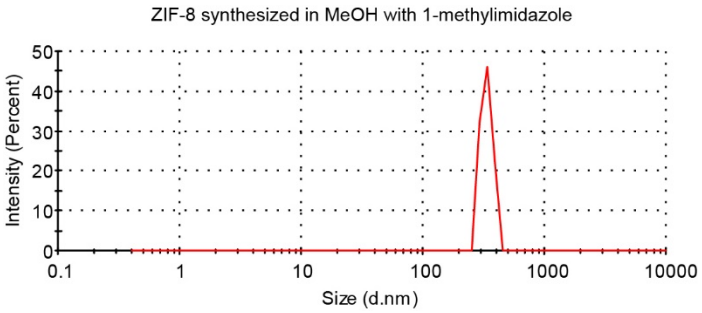

Fig. S5. DLS size distribution of ZIF-8 (synthesized with 1-methylimidazole) in MeOH dispersion.

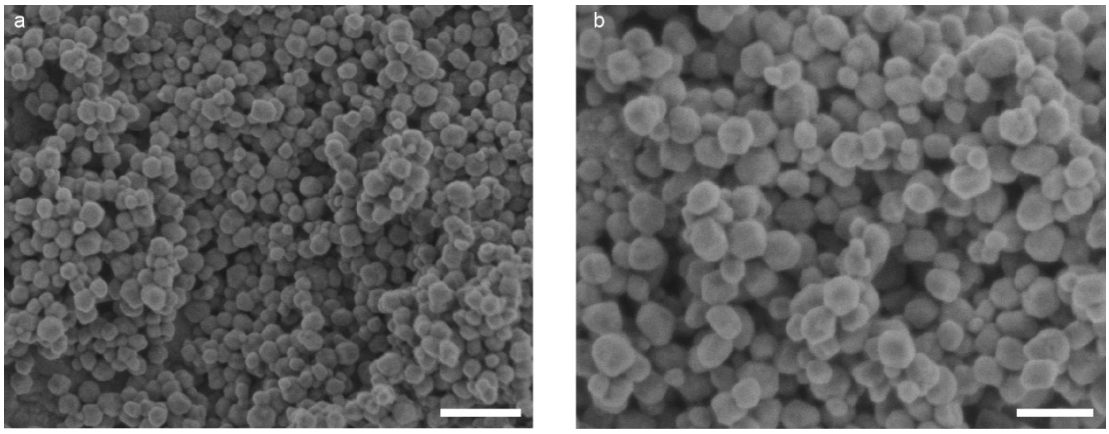

Fig. S6. SEM images of ZIF-7 nanocrsytals, scale bar, 200 nm (a) and 100 nm (b).

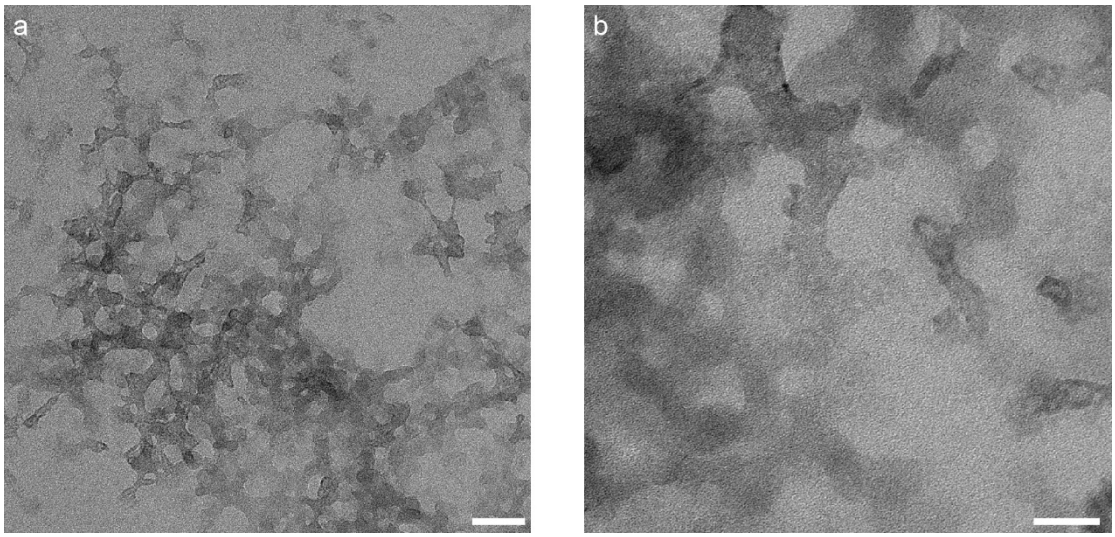

Fig. S7. TEM images of ZIF-8 synthesized with n-butylamine, scale bar, 50 nm (a) and 20 nm (b).

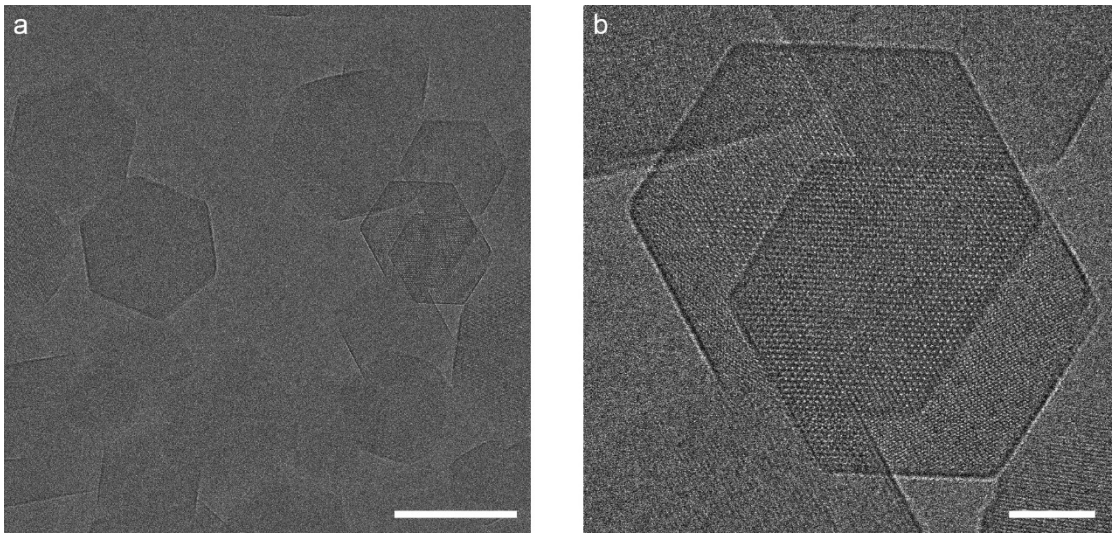

Fig. S8. TEM images of ZIF-8 synthesized in static state, scale bar, 100 nm (a) and 20 nm (b).

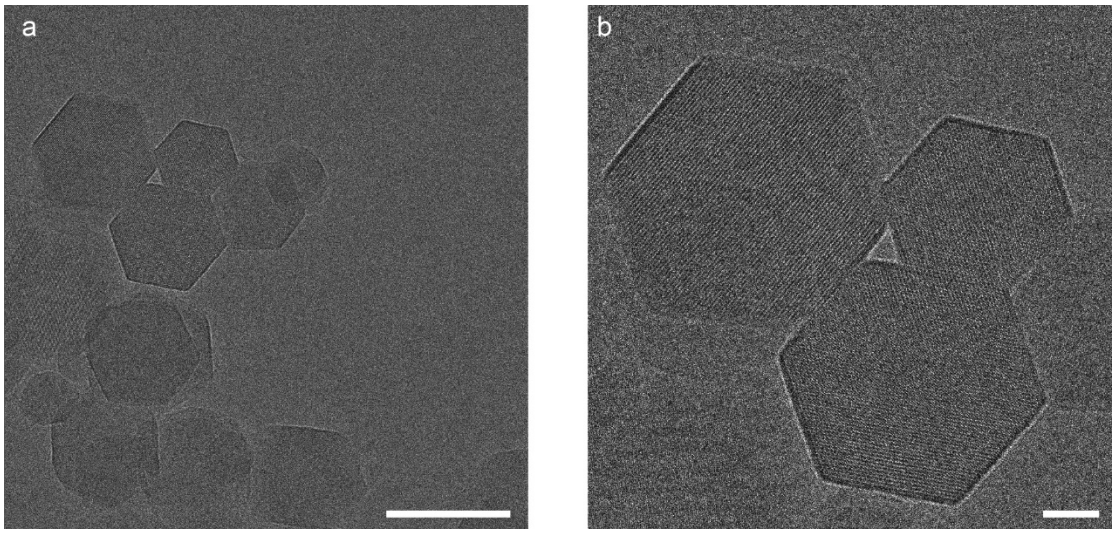

Fig. S9. TEM images of ZIF-8 synthesized by stirring for 3 h, scale bar, 100 nm (a) and 20 nm (b).

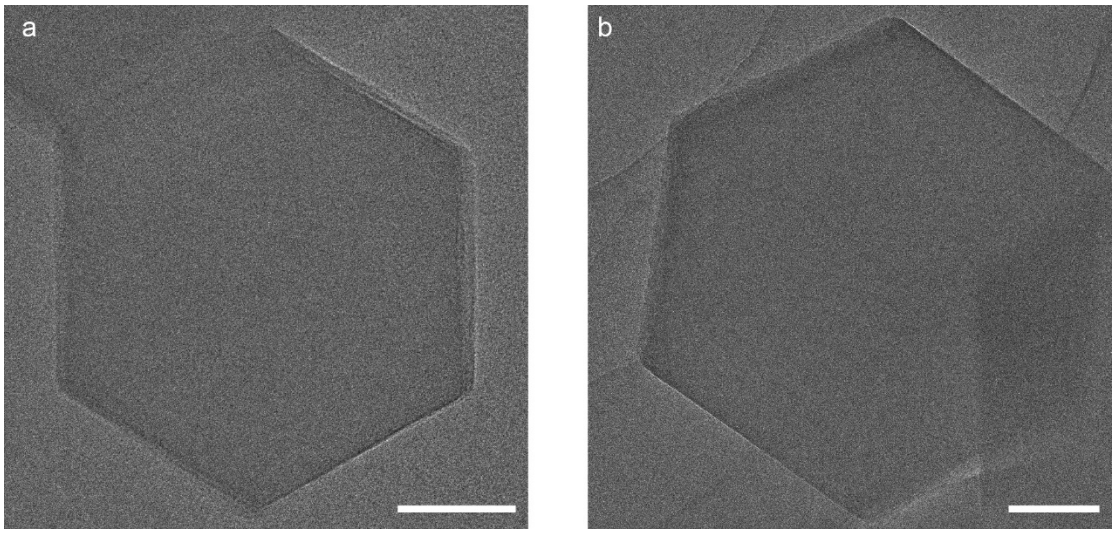

Fig. S10. TEM images of ZIF-8 synthesized with zinc acetate and 1-methylimidazole, respectively. Scale bar, 50 nm (a) and 100 nm (b).

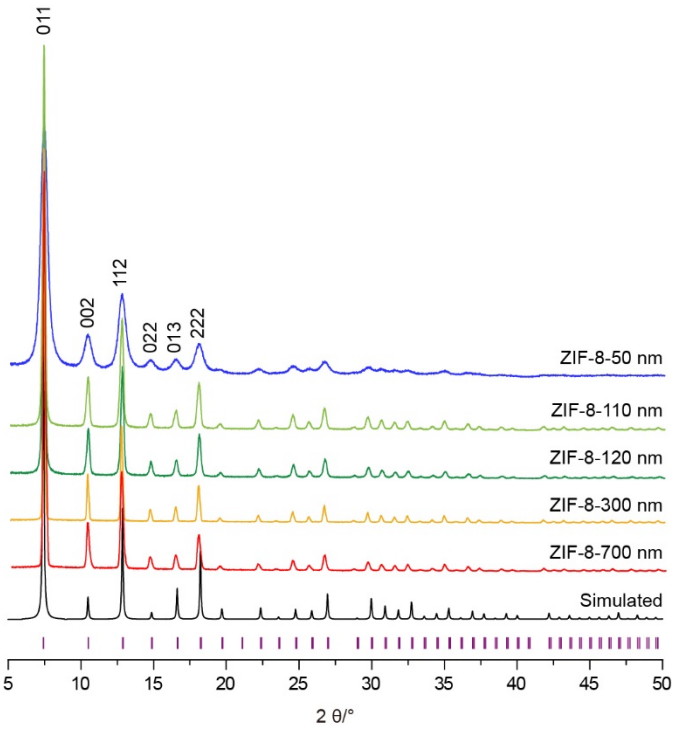

Fig. S11. Comparisons of the experimental PXRD pattern of activated ZIF-8 in different particle sizes (50, 110, 120, 300 and 700 nm), with the simulated diffraction pattern (black) (Cu Kα λ=1.5406 Å).

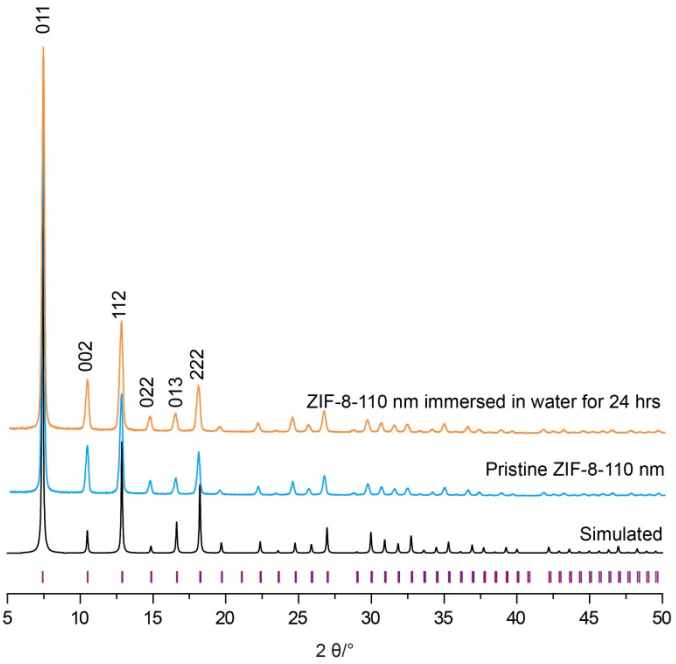

Fig. S12. PXRD patterns of ZIF-8 (110 nm) collected during stability test in water at room temperature for 24 h. The framework structure of ZIF-8 was unchanged after 24 h.

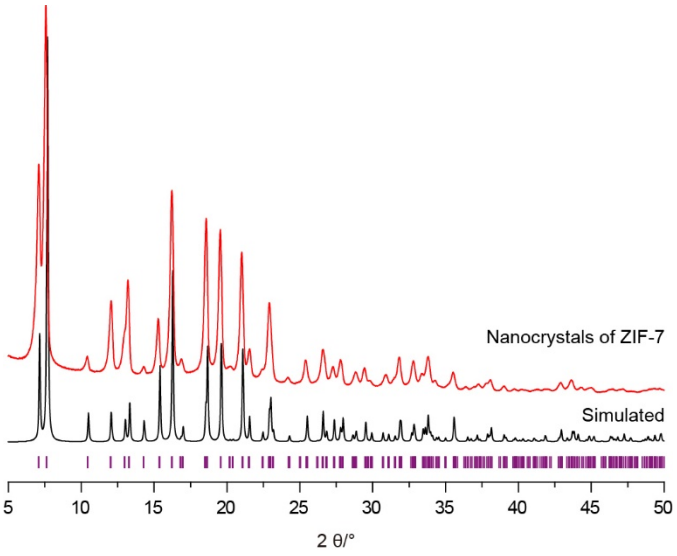

Fig. S13. Comparisons of the experimental PXRD pattern of activated ZIF-7 nanocrystal, with the simulated diffraction pattern (black) (Cu Kα λ=1.5406 Å).

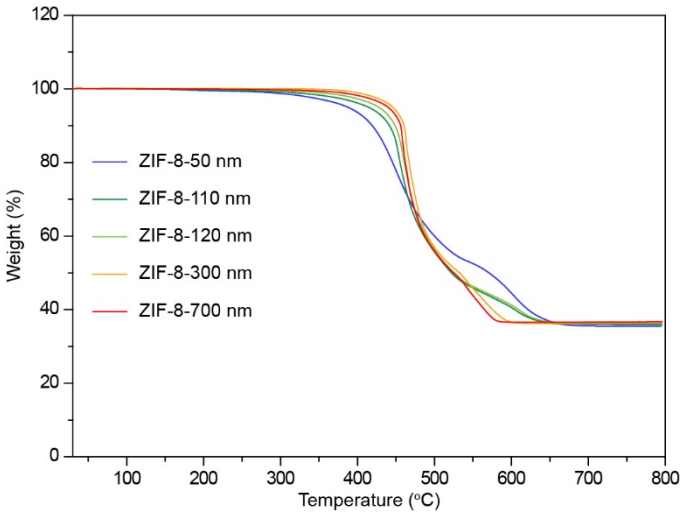

Fig. S14. Thermo gravimetric analysis (TGA) trace of activated ZIF-8. In each TGA plot, the small weight loss before 100 °C was attributed to the evaporation of water introduced into MOF from air during the sample mounting. The major weight loss evidenced (around 450 °C) was caused by the destruction of ZIF series. The thermal stability of these ZIF-8 samples was demonstrated by TGA in air where no obvious structure decomposition was observed until 450 °C.

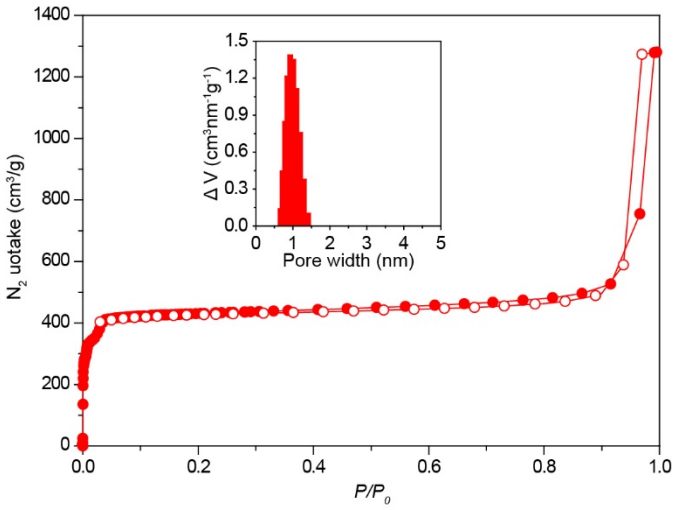

Fig. S15. Nitrogen isotherm of ZIF-8 (synthesized with $Zn(NO_3)_2 \bullet 6H_2O$ by stirring in MeOH) at 77 K. Filled and open symbols represent adsorption and desorption branches, respectively. Points are connected to provide clear shape of the isotherm. Inserted plot shows the pore size distribution of ZIF-8.

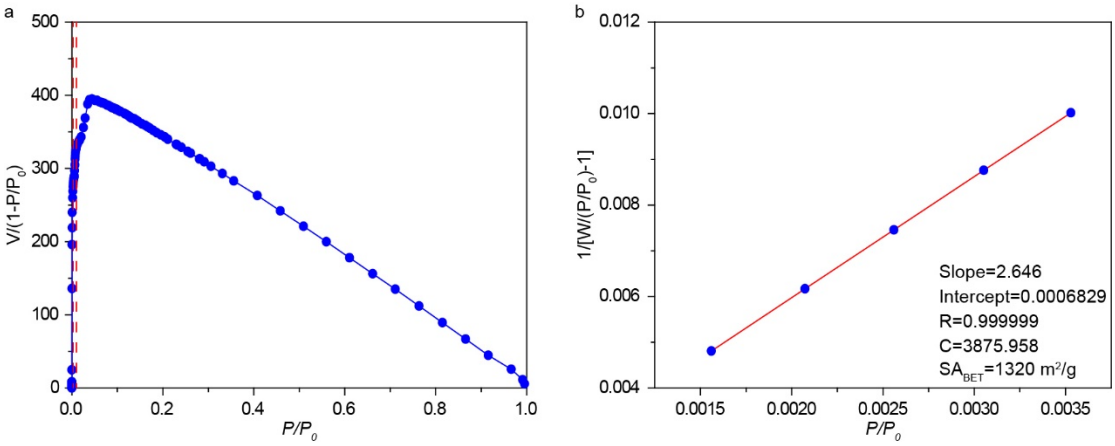

Fig. S16. BET area calculation for ZIF-8 (synthesized with $Zn(NO_3)_2$•$6H_2O$ by stirring in MeOH) from simulated nitrogen isotherm at 77 K. (a) Only points between the dashed lines are selected based on the first consistency criterion, (b) Plot of the linear P/P_0 range.

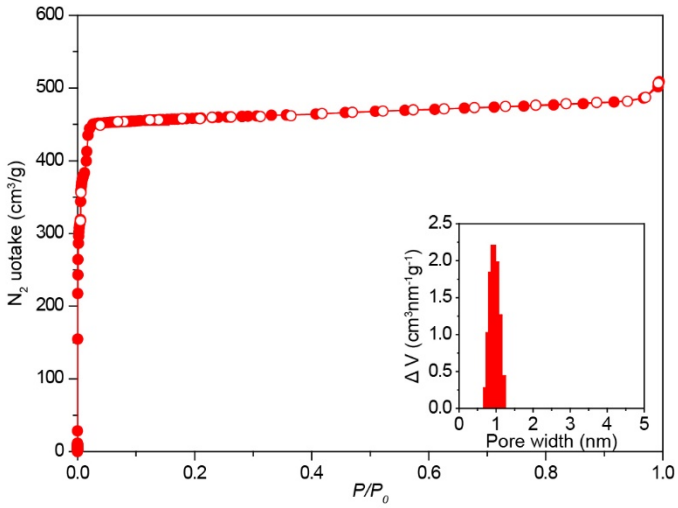

Fig. S17. Nitrogen isotherm of ZIF-8 (synthesized with $Zn(OAc)_2 \cdot 2H_2O$ by stirring in MeOH) at 77 K. Filled and open symbols represent adsorption and desorption branches, respectively. Points are connected to provide clear shape of the isotherm. Inserted plot shows the pore size distribution of ZIF-8.

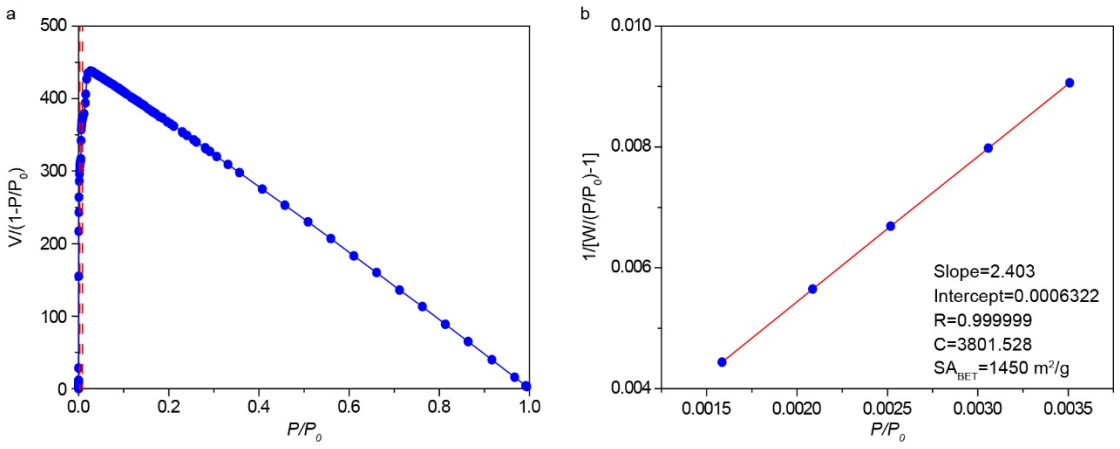

Fig. S18. BET area calculation for ZIF-8 (synthesized with $Zn(OAc)_2 \bullet 2H_2O$ by stirring in MeOH) from simulated nitrogen isotherm at 77 K. (a) Only points between the dashed lines are selected based on the first consistency criterion, (b) Plot of the linear P/P_0 range.

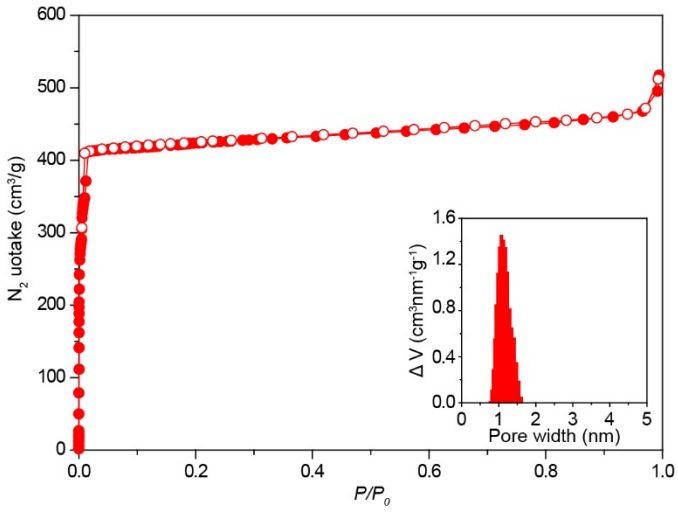

Fig. S19. Nitrogen isotherm of ZIF-8 (synthesized with 1-methylimidazole) at 77 K. Filled and open symbols represent adsorption and desorption branches, respectively. Points are connected to provide clear shape of the isotherm. Inserted plot shows the pore size distribution of ZIF-8.

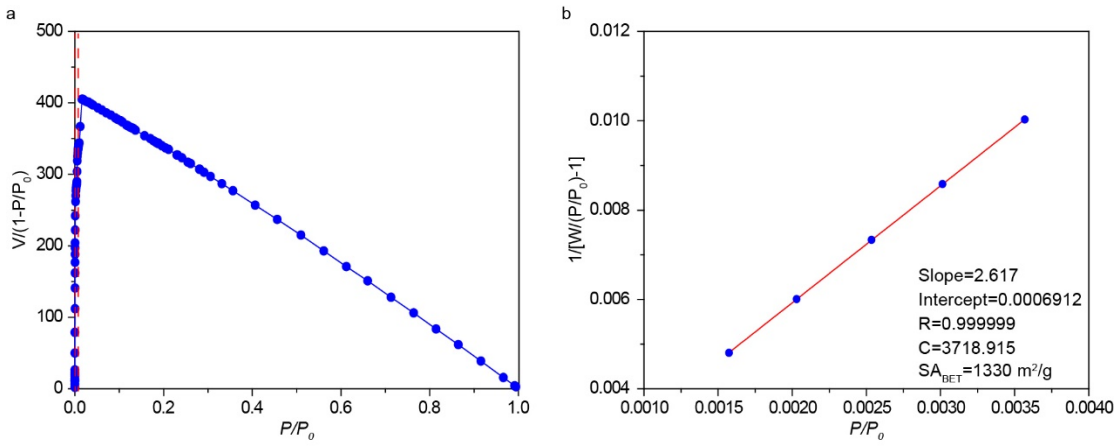

Fig. S20. BET area calculation for ZIF-8 (synthesized with 1-methylimidazole) from simulated nitrogen isotherm at 77 K. (a) Only points between the dashed lines are selected based on the first consistency criterion, (b) Plot of the linear P/P_0 range.

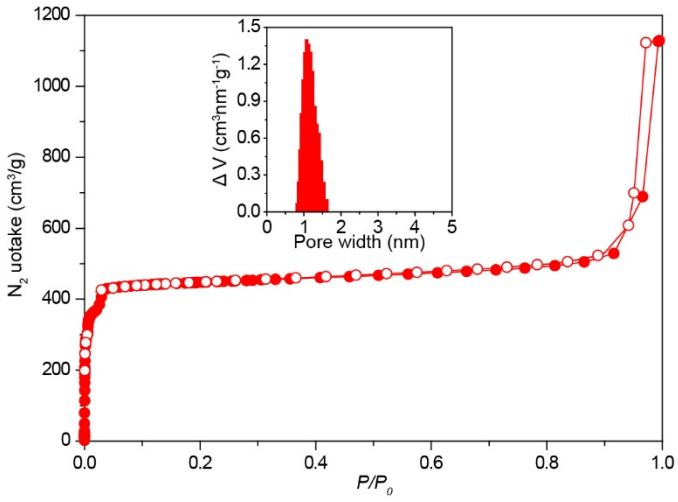

Fig. S21. Nitrogen isotherm of ZIF-8 (synthesized with $Zn(NO_3)_2 \cdot 6H_2O$ static for 24 h) at 77 K. Filled and open symbols represent adsorption and desorption branches, respectively. Points are connected to provide clear shape of the isotherm. Inserted plot shows the pore size distribution of ZIF-8.

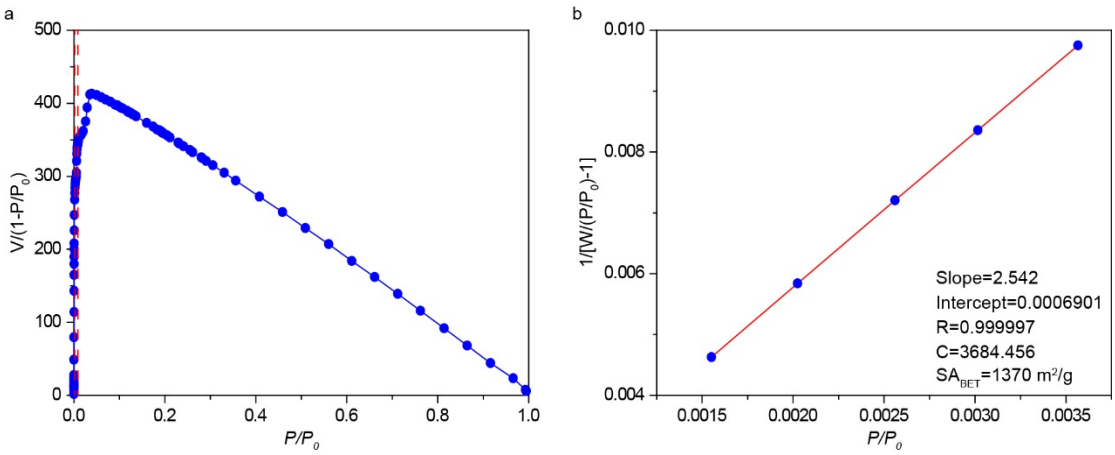

Fig. S22. BET area calculation for ZIF-8 (synthesized with $Zn(NO_3)_2$•$6H_2O$ static for 24 h) from simulated nitrogen isotherm at 77 K. (a) Only points between the dashed lines are selected based on the first consistency criterion, (b) Plot of the linear P/P_0 range.

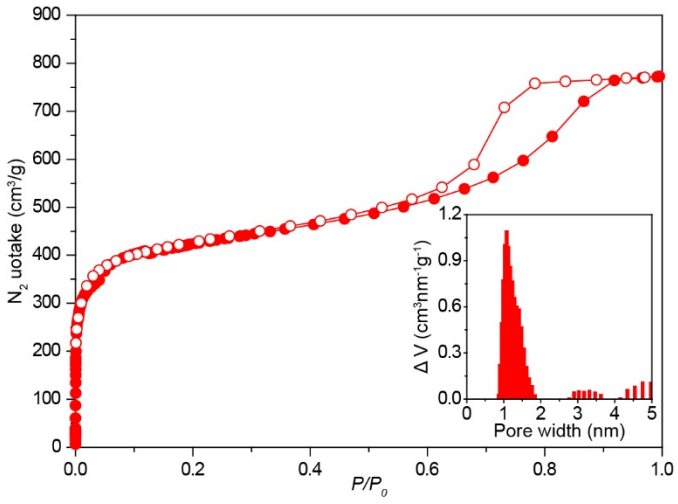

Fig. S23. Nitrogen isotherm of ZIF-8 (synthesized with n-butylamine) at 77 K. Filled and open symbols represent adsorption and desorption branches, respectively. Points are connected to provide clear shape of the isotherm. Inserted plot shows the pore size distribution of ZIF-8.

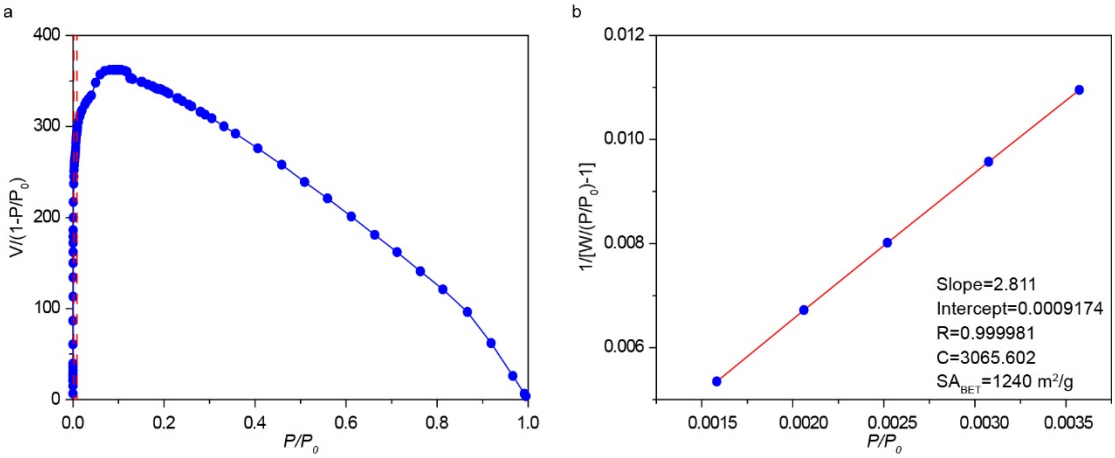

Fig. S24. BET area calculation for ZIF-8 (synthesized with n-butylamine) from simulated nitrogen isotherm at 77 K. (a) Only points between the dashed lines are selected based on the first consistency criterion, (b) Plot of the linear P/P_0 range.

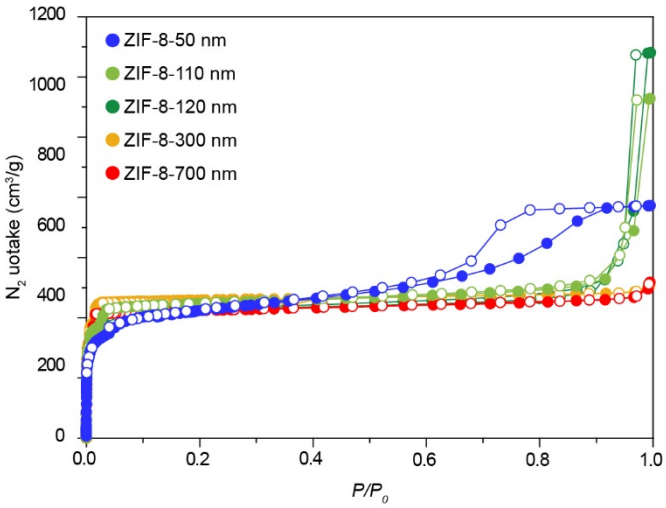

Fig. S25. Nitrogen isotherm of ZIF-8 in different sizes at 77 K. Filled and open symbols represent adsorption and desorption branches, respectively. Points are connected to provide clear shape of the isotherm.

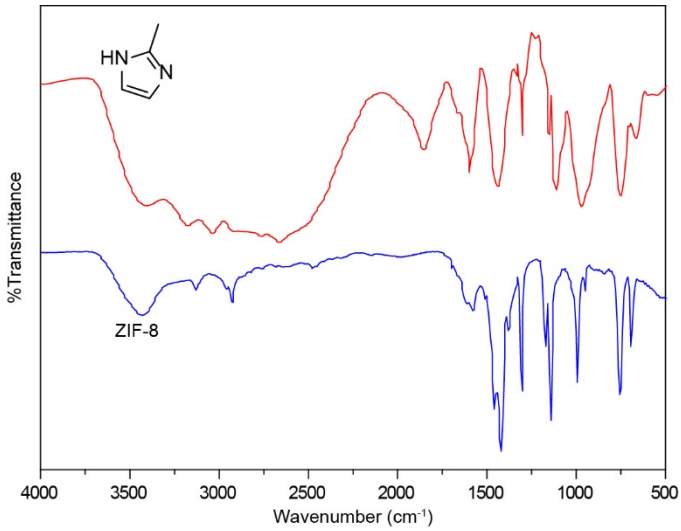

Fig. S26. IR spectra of ZIF-8 nanocrystals and 2-methylimidazole.

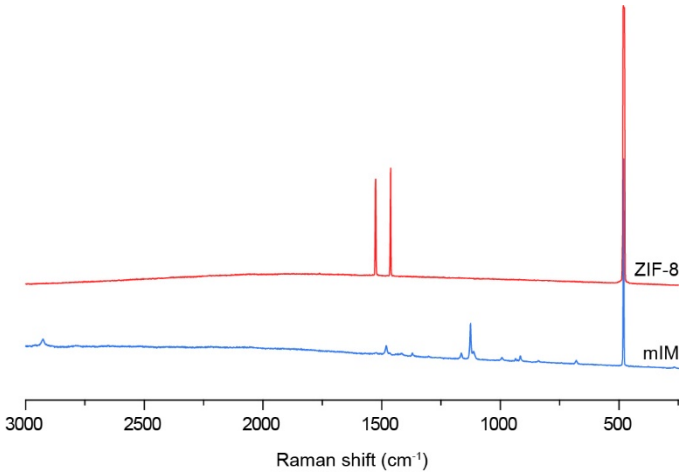

Fig. S27. Raman spectra of ZIF-8 nanocrystals and 2-methylimidazole.

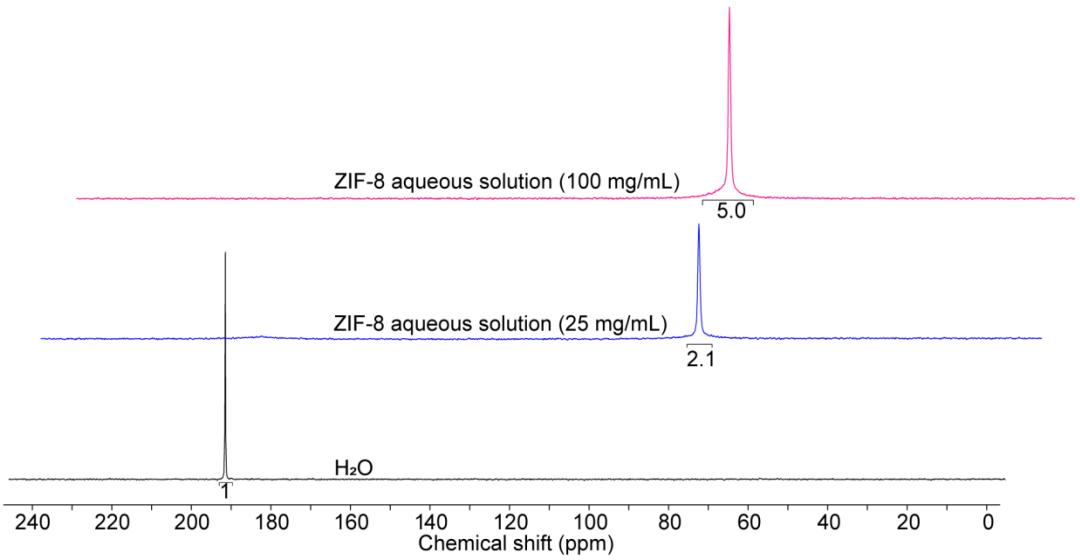

Fig. S28. Hyperpolarized ^{129}Xe NMR spectra for pure water and ZIF-8 aqueous solution (25 mg/mL and 100 mg/mL). NS=16, LB=10 Hz. For these spectra, the zg sequence was applied for acquisition (rectangular pulse, the pulse length p1=31.8 μs). The ^{129}Xe NMR signal intensity (NMR signal integral) of loaded Xe in ZIF-8 is stronger than dissolved Xe in water by more than 4-fold.

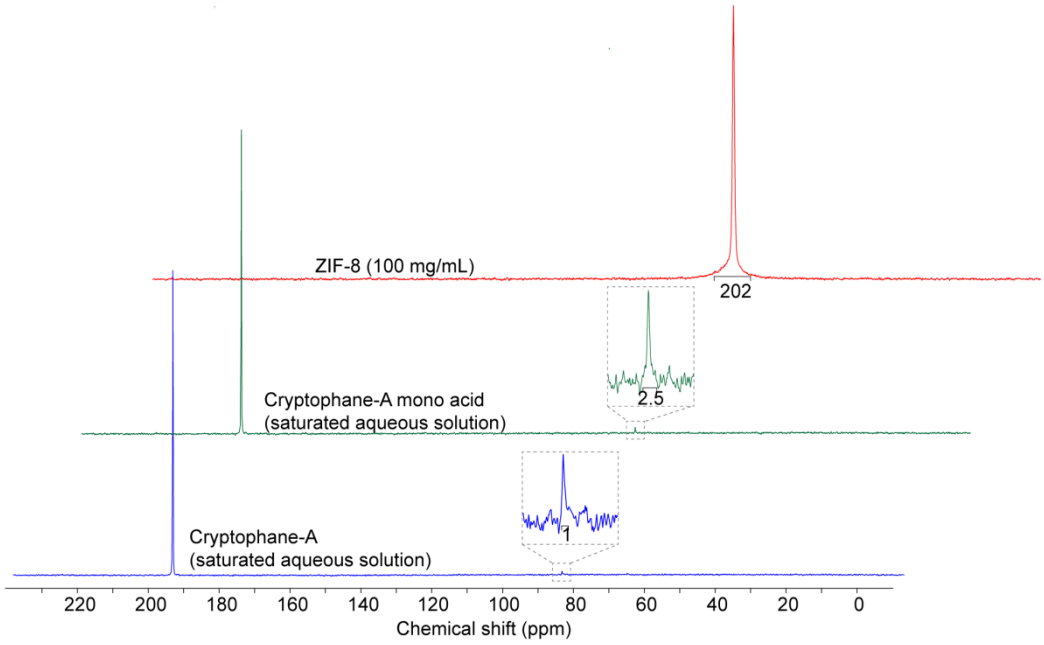

Fig. S29. Hyperpolarized ^{129}Xe NMR spectra for cryptophane-A (CrypA) (saturated aqueous solution), cryptophane-A mono acid (saturated aqueous solution) and ZIF-8 aqueous solution (100 mg/mL). For these spectra, the zg sequence was applied for acquisition (rectangular pulse, the pulse length p1=31.8 μs). NS=16, LB=10 Hz. The signal intensity (NMR signal integral) of hyperpolarized ^{129}Xe entrapped in ZIF-8 is 80 times that CrypA modified with one carboxylate group, and 200 times that of pristine CrypA.

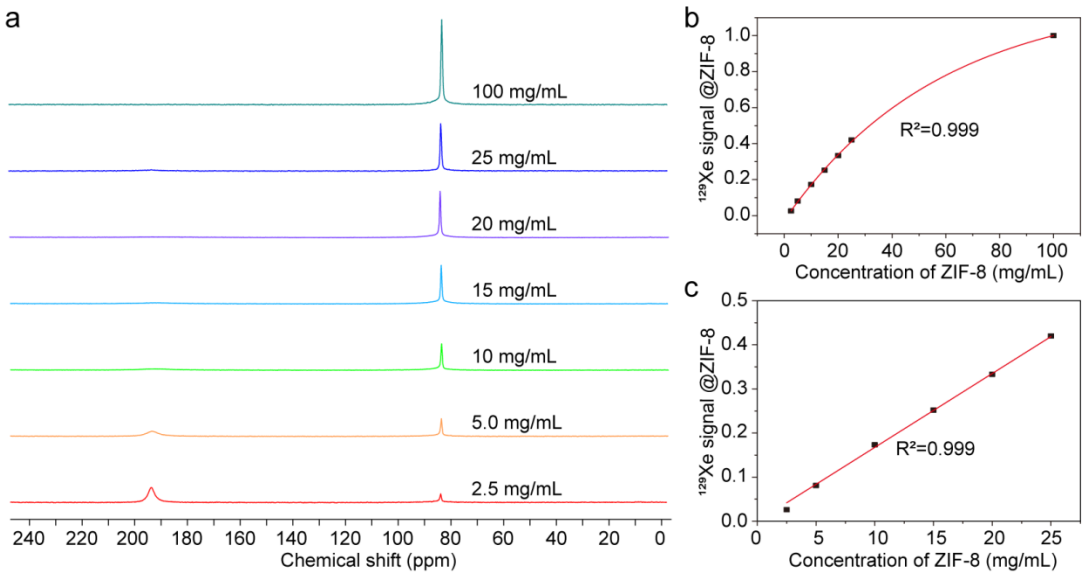

Fig. S30. (a) NMR spectra of hyperpolarized ^{129}Xe in ZIF-8 (110 nm) at different concentration (2.5, 5.0, 10, 15, 20, 25, and 100 mg/mL) in aqueous solution. (b) and (c) The concentration dependent entrapped ^{129}Xe NMR signal intensity (NMR signal integral). For these spectra, the zg sequence was applied for acquisition (rectangular pulse, the pulse length p1=31.8 μs). NS=16, LB=10 Hz.

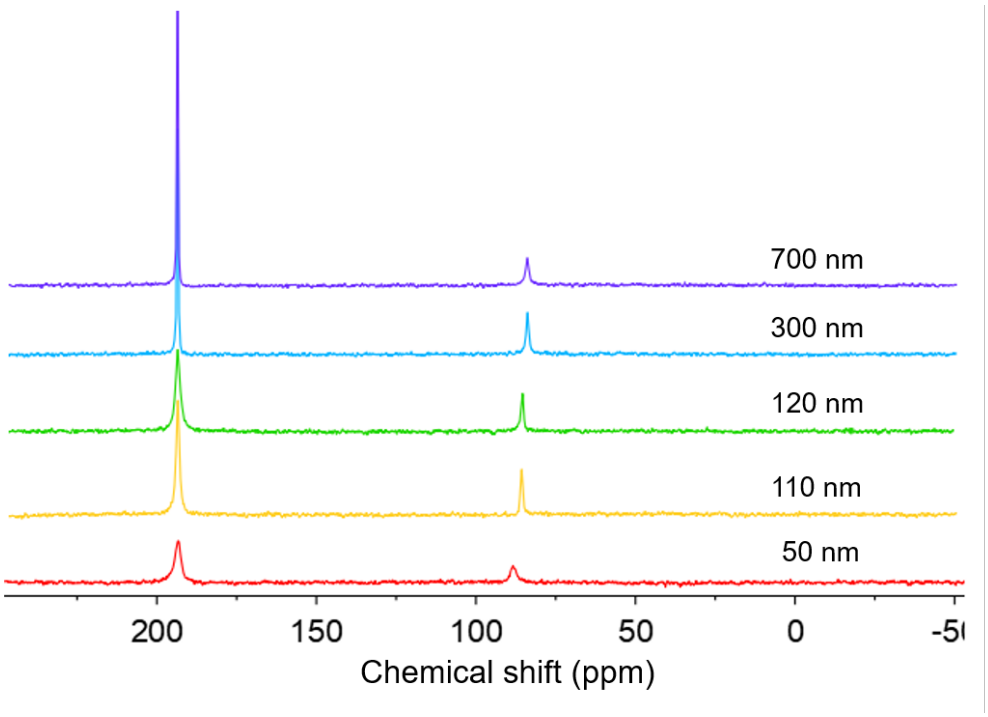

Fig. S31. Hyperpolarized ^{129}Xe NMR spectra for different sizes of ZIF-8 in aqueous solution, all the concentration of ZIF-8 are 2.5 mg/mL. For these spectra, the zg sequence was applied for acquisition (rectangular pulse, the pulse length p1=31.8 μs). NS=32, LB=15 Hz.

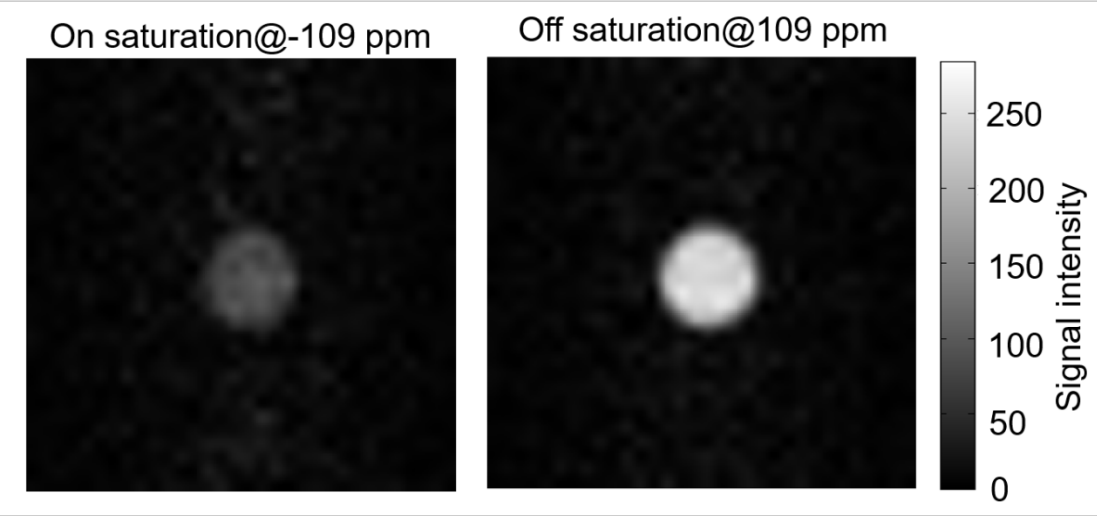

Fig. S32. Hyper-CEST image showing the average of 16 on-resonant (-109 ppm, relative to dissolved Xe in solution at 0 ppm, left) and 16 off-resonant (109 ppm, relative to dissolved Xe in solution at 0 ppm, right) scans. The image was acquired using a RARE sequence with 16 averages for each on- and off-resonant image (slice thickness=30 mm, matrix size=32×32, FOV=30×30 mm^2, in-plane resolution=0.9375×0.9375 mm^2, bandwidth=5400 Hz, echo time=4.97 ms, repetition time=82.3 ms, no partial Fourier transform acceleration, rare factor=8).

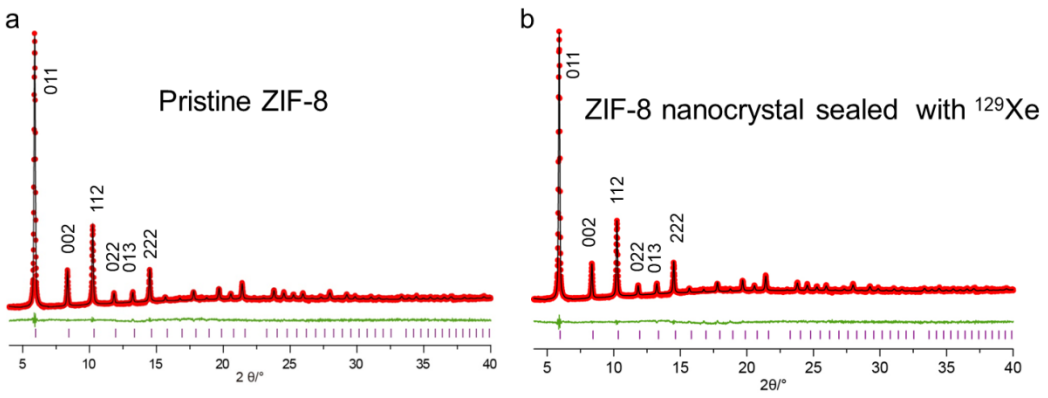

Fig. S33. (a and b) PXRD pattern of pristine ZIF-8 and ^{129}Xe loaded ZIF-8. Wavelength of X-ray sources, λ= 1.24 Å. The experimental (red), refined (black) and difference (green) patterns are displayed. The Bragg positions are marked as pink bars.

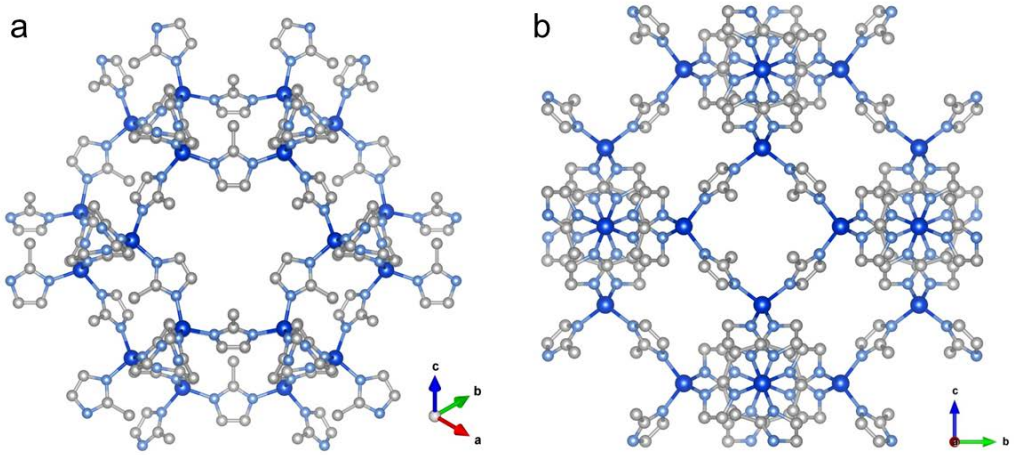

Fig. S34. Visualization of pristine ZIF-8. (a) Along [111] axis and (b) along [100] axis. Carbon (white), nitrogen (light blue) and zinc (blue).

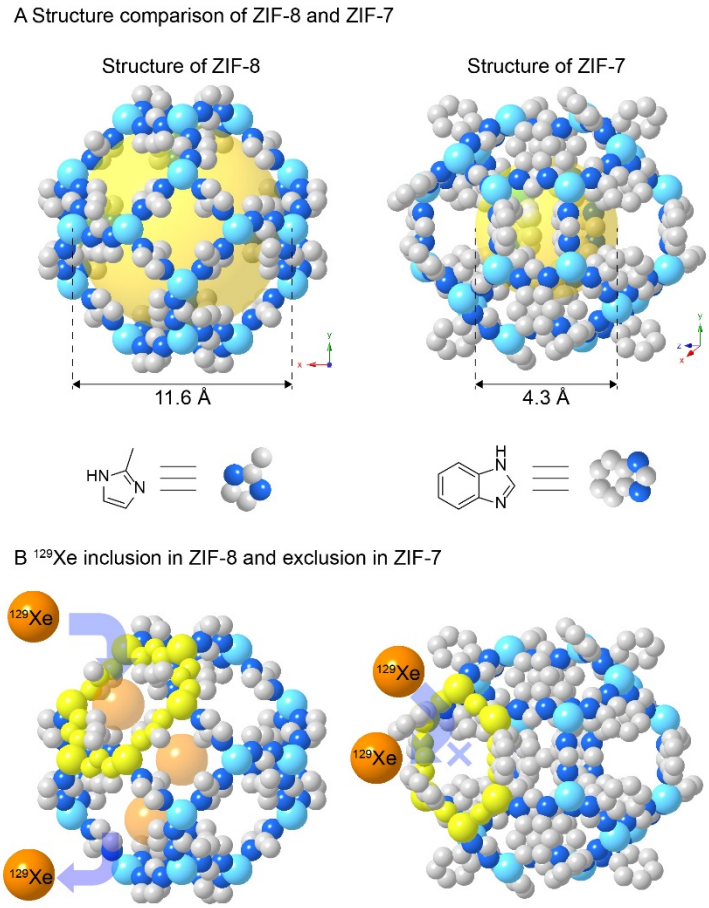

Fig. S35. Structure construction of ZIF-8 and ZIF-7 in sod topology. (A) Unit cell structure of ZIF-8 and ZIF-7. (B) ^{129}Xe is compatible with the window size of ZIF-8, while the diameter of ^{129}Xe is too large for ZIF-7.

Table S1. Particle size distribution analysis. Based on the dynamic light scattering (DLS) results, the hydrodynamic diameter of ZIF-8 ranges from 50 nm to 700 nm. The particles of nanocrystals were around 50-300 nm with low PDI values, indicating uniform sizes for nano-sized ZIF-8.

Nanocrystals	Hydrodynamic diameter in MeOH (nm)	PDI	Modulator
ZIF-8	53.0±0.50	0.164	*n*-butylamine
ZIF-8	107.6±0.32	0.068	none
ZIF-8	117.5±1.30	0.057	none
ZIF-8	275.7±6.30	0.344	none
ZIF-8	641.3±27.17	0.604	1-methylimidazole

Table S2. Property summary of ZIF-8 in different sizes.

Crystal size (nm)	Zeta potential (mV)	BET SA (m^2/g)
50	16.9±0.34	1240
110	22.9±0.59	1370
120	23.9±0.39	1320
300	12.1±0.33	1450
700	22.5±0.21	1330

Table S3. Characteristics of different xenon host. When compared with other xenon host molecule, such as CrypA, CB6, gas vesicles, nanoemulsion, β-lactamase, Fe_4L_6 and so on, ZIF-8 is a cheaper xenon host with higher efficiency.

Host	$\delta_{entrapped\ Xe}$ (ppm)	Δδ (ppm)	K (M^{-1})	Cost
ZIF-8 (our work)	~84	109	N/A	~74 $/g
CrypA (5a)	~62	131	~4000	~1700 $/g
CB6 (5b)	~110	83	~2500	~120 $/g
Nanoemulsion (5c)	~110	83	N/A	N/A
Gas vesicles (5d)	~20	173	N/A	N/A
β-lactamase (5e)	~260	67	N/A	N/A
Fe_4L_6 (5f)	~203	10	~16	N/A

Table S4. Characteristics of different sizes of ZIF-8.

Size (nm)	Δδ (ppm)	SNR (^{129}Xe@ZIF-8)	FWHM (Hz) (^{129}Xe@ZIF-8)	FWHM (Hz) (^{129}Xe@H_2O)
~50	105.6	14	295	259
~110	109.9	28	118	156
~120	110.5	25	126	210
~300	111.9	30	134	65
~700	111.7	21	160	58

SI References

1. (a) R. Banerjee *et al.*, High-throughput synthesis of zeolitic imidazolate frameworks and application to CO_2 capture. *Science* **319**, 939-943 (2008). (b) Y. Pan, Y. Liu, G. Zeng, L. Zhao, Z. Lai, Rapid synthesis of zeolitic imidazolate framework-8 (ZIF-8) nanocrystals in aqueous system. *Chem. Commun*. **47**, 2071-2073 (2011). (c) J. Cravillon *et al*., Controlling zeolitic imidazolate framework nano-and microcrystal formation: insight into crystal growth by time-resolved in situ static light scattering. *Chem. Mater.* **23**, 2130-2141 (2011). (d) A. Schejn *et al.*, Controlling ZIF-8 nano- and microcrystal formation and reactivity through zinc salt variations. *CrystEngComm* **16**, 4493-4500 (2014).
2. K. S. Walton, R. Q. Snurr, Applicability of the BET method for determining surface areas of microporous metal-organic frameworks. *J. Am. Chem. Soc.* **129**, 8552-8556 (2007).
3. (a) X. Chen *et al*., Direct observation of Xe and Kr adsorption in a Xe-selective microporous metal-organic framework. *J. Am. Chem. Soc*. **137**, 7007-7010 (2015). (b) X. Feng *et al.*, Kr/Xe separation over a chabazite zeolite membrane. *J. Am. Chem. Soc*. **138**, 9791-9794 (2016). (c) Y. Hu, Z. Liu, J. Xu, Y. Huang, Y. Song, Evidence of pressure enhanced CO_2 storage in ZIF-8 probed by FTIR spectroscopy. *J. Am. Chem. Soc*. **135**, 9287-9290 (2013).
4. C. Zhang *et al.*, Unexpected molecular sieving properties of zeolitic imidazolate framework-8. *J. Phys. Chem. Lett.* **3**, 2130-2134 (2012).
5. (a) M. M. Spence *et al.*, Functionalized xenon as a biosensor. *Proc. Natl. Acad. Sci. USA.* **98**, 10654-10657 (2001). (b) M. Kunth, C. Witte, A. Hennig, L. Schröder, Identification, classification, and signal amplification capabilities of high-turnover gas binding hosts in ultra-sensitive NMR. *Chem. Sci.* **6**, 6069-6075 (2015). (c) T. K. Stevens, R. M. Ramirez, A. Pines, Nanoemulsion contrast agents with sub-picomolar sensitivity for xenon NMR. *J. Am. Chem. Soc.* **135**, 9576-9579 (2013). (d) M. G. Shapiro *et al*., Genetically encoded reporters for hyperpolarized xenon magnetic resonance imaging. *Nat. Chem.* **6**, 629-634 (2014). (e) Y. Wang, B. W. Roose, E. J. Palovcak, V. Carnevale, I. J. Dmochowski, A genetically encoded β-lactamase reporter for ultrasensitive ^{129}Xe NMR in mammalian cells. *Angew. Chem. Int. Ed.* **55**, 8984-8987 (2016). (f) J. Roukala *et al*., Encapsulation of xenon by a self-assembled Fe_4L_6 metallosupramolecular cage. *J. Am. Chem. Soc*. **137**, 2464-2467 (2015).